

High-order above-threshold ionization beyond the electric dipole approximation: Dependence on the atomic and molecular structure

Simon Brennecke and Manfred Lein*

Institut für Theoretische Physik, Leibniz Universität Hannover, Appelstraße 2, 30167 Hannover, Germany

(Received 5 October 2018; published 13 December 2018)

We provide an in-depth analysis of high-order above-threshold ionization of atoms and molecules by strong laser pulses, using three different theoretical approaches beyond the electric dipole approximation: (i) the numerical solution of the time-dependent Schrödinger equation, (ii) the classical three-step model, and (iii) the quantum-orbit model. In the classical and quantum-orbit models, we include an accurate description of the rescattering step by target-specific differential scattering cross sections. The considerable forward shift of the photoelectron momentum distributions along the laser propagation direction can be understood in terms of the nondipole electron motion after rescattering. An explanation of the additionally observed forward-backward asymmetry of the signal strength requires the accurate modeling of the rescattering step and the electron dynamics before the rescattering event. For the H_2^+ molecular ion, we compare the cases of parallel and perpendicular alignment of the molecular axis and we show that the interference pattern and its modification due to the nondipole effects are orientation dependent. Compared to atoms, the nondipole effects in molecular high-order above-threshold ionization appear more pronounced and amenable to experimental observation.

DOI: [10.1103/PhysRevA.98.063414](https://doi.org/10.1103/PhysRevA.98.063414)

I. INTRODUCTION

Over the past decades, many ultrafast imaging methods using the recollision of laser-ionized bursts of coherent electron wave packets have been developed to self-probe atomic or molecular structure and dynamics on its subfemtosecond time scale [1]. In principle, every observable that is influenced by the electron recollision can be used to obtain structural information, e.g., fragment kinetic energy release from molecules [2] and high-harmonic generation spectra [3–6]. The improvements in the velocity-map imaging technique [7] and in the cold-target recoil-ion momentum spectroscopy [8] made it possible to use directly photoelectron momentum distributions of the rescattered electrons suggested in Refs. [9,10] for imaging molecules. This so-called laser-induced electron diffraction (LIED) technique has been successfully used to probe the structure of static atoms and molecules [11,12] as well as nuclear and also electronic valence-shell dynamics in molecules [13,14].

The physical basis of LIED is formed by high-order above threshold ionization (HATI). In this process, the ionized electron absorbs many more photons than the minimum number necessary for ionization, leading to a characteristic appearance of peaks in the energy spectrum separated by the photon energy [15]. In the simplest possible picture, the “direct” electrons can be described in a two-step model consisting of (i) laser-induced ionization and (ii) potential-free acceleration of the electron as a classical particle in the laser field [16,17]. Depending on the ionization times some electrons are driven back to the parent ion during their acceleration

and they may scatter elastically off the potential before they are subsequently accelerated in the field for a second time. This process leads to the high-energy electrons in HATI that form a plateau in the energy spectrum reaching up to the $\approx 10U_p$ cutoff [18,19], where $U_p = E_0^2/(4\omega^2)$ is known as the pondermotive potential for a linearly polarized laser field with amplitude E_0 and frequency ω . (We use atomic units unless otherwise stated.) The return of the electron to the parent ion is called the recollision step. Hence, motivated by the earlier proposed model for high-harmonic generation [20,21], we speak of the three-step model of HATI.

However, in order to interpret the emission strength of the momentum distributions more complex, quantum-mechanical theories including the scattering step properly have to be used. As the *ab initio* study by the numerical solution of the time-dependent Schrödinger equation (TDSE) is only possible for a small number of electrons, approximate theories are needed that additionally help to understand the underlying physical processes. A starting point is often the strong-field approximation (SFA) which was originally formulated for direct electrons in Refs. [22–24]. Here, it is assumed that once the electron has been released, its motion is fully governed by the laser field and the influence of the ionic potential is neglected. The rescattering off ionic potentials has been included in the context of SFA by means of a Born series where the first-order term in the binding potential is often called improved SFA (ISFA) [25,26]. The application of the saddle-point method allows a fruitful analytical treatment known as the quantum-orbit model (QOM) [27,28], which provides an intuitive description of the strong-field processes. The neglect of “distortion” of the incident plane wave caused by the potential in the first Born approximation (1BA) limits the reliability range of ISFA depending on the energy of the recolliding electron, the

*lein@itp.uni-hannover.de

shape of the potential, and the dimensionality of the problem. In three dimensions the IBA yields the correct differential cross section (DCS) for a bare Coulomb potential, but it is not exact if the potential includes a short-range contribution as it is usually the case for optimized single-electron effective potentials. To improve the laser-assisted rescattering beyond the IBA we follow the low-frequency approximation that has been invented for laser-assisted electron-atom scattering by Kroll and Watson [29] and introduced to the context of HATI by Milošević [30,31]. Within this theoretical framework it is possible to give a derivation of the factorization of HATI amplitudes in products of the field-free elastic scattering DCS σ and a factor describing the returning wave packet. After additional approximations, this leads to the quantitative rescattering theory (QRS) [32,33]. For diatomic molecules, the two-center interference influences strongly the DCS and the resulting minimum in the momentum distribution [34,35] can be used to reconstruct bond lengths [13].

In nearly all theoretical calculations of HATI, the electric dipole approximation is used, where it is assumed that the incident electric field is spatially homogeneous over the field-target interaction region and furthermore the magnetic field is completely neglected. Thus, for ionization of a spherically symmetric system, the photoelectron momentum distribution has to be symmetric under interchange of the forward and backward directions and no radiation-pressure effects take place. Here, “forward” denotes the laser propagation direction. However, in a few experiments focusing on “direct” (nonrescattered) as well as low-energy rescattered electrons, the transfer of photon momentum to the photoelectrons has been observed by Smeenk *et al.* [36], Ludwig *et al.* [37], and Maurer *et al.* [38]. The experimental findings have been analyzed in different theoretical frameworks ranging from the numerical solution of the TDSE beyond the dipole approximation [39,40] over nondipole versions of the strong-field approximation [41–45] to trajectory-based simulations [46]. The nondipole work on strong-field dynamics including recollision mostly focused on high-harmonic generation [47–51] or considered HATI for quite high intensities beyond those used in typical table-top experiments [52,53]. Recently, we presented the HATI results from the numerical solution of the nondipole TDSE in the regime of moderate laser intensities [54]. Our central findings were a deformation of the momentum distribution shape, which can be explained in terms of a nondipole three-step model, and an additional forward-backward asymmetry in the emission strength, which turned out to be outside the scope of the three-step model.

Our goal in the present paper is to investigate the nondipole effects in HATI and especially the observed asymmetry in more detail. To this end, we present results from the numerical solution of the nondipole TDSE for an atomic helium model and a model of the H_2^+ molecular ion. Expanding our nondipole three-step model by treating the scattering step properly, the asymmetry is analyzed qualitatively. A nondipole version of the low-frequency approximation and corresponding quantum-orbit model is derived to interpret quantitatively the whole photoelectron momentum distributions in the high-energy rescattering regime for short-range potentials. In addition, we discuss the shortcomings of our quantum-orbit model for long-range potentials with

Coulombic tails. Finally, the nondipole modifications of the two-center molecular interference pattern in H_2^+ are analyzed with the help of the classical three-step model.

II. METHODS

A. Physical setup

We consider the ionization process of a single-active-electron model under the influence of a linearly polarized plane-wave laser pulse of three cycle duration, fully represented by the electric field

$$\mathbf{E}(\mathbf{r}, t) = \mathbf{E}(\eta) = -E_0 \sin^2(\omega\eta/6) \cos(\omega\eta) \mathbf{e}_x, \quad (1)$$

with the retarded time $\eta = t - z/c$. The incident pulse travels in z direction with speed of light $c = 1/\alpha \approx 137$. The used frequency of $\omega = 0.056$ a.u. corresponds to 814 nm wavelength and the field strength of $E_0 = 0.151$ a.u. corresponds to an intensity of 8.0×10^{14} W/cm². The electric field points along the x axis of the coordinate system and the corresponding magnetic field $\mathbf{B} = \mathbf{e}_z \times \mathbf{E}/c$ points along the y axis. In the used Coulomb gauge the electromagnetic scalar potential is chosen to be zero and the vector potential $\mathbf{A}(\mathbf{r}, t) = \mathbf{A}(\eta)$ is related to the physical fields by $\mathbf{E} = -\partial_t \mathbf{A}$ and $\mathbf{B} = \nabla \times \mathbf{A}$. For the laser parameters under consideration, an expansion of the vector potential in $1/c$ can be applied:

$$\mathbf{A}(\mathbf{r}, t) \approx \mathbf{A}(t) + z/c \mathbf{E}(t). \quad (2)$$

Compared to the dipole approximation this leading-order correction in $1/c$ results in a linear position dependence of the electric field and a spatially homogeneous magnetic field such that all considered effects are described in electric quadrupole and magnetic dipole approximation.

In two dimensions, we model the helium atom with two different single-active electron potentials: (i) a long-range soft-core potential

$$V_C(r) = -\frac{e^{-0.575r} + 1}{\sqrt{r^2 + 0.75}}, \quad (3)$$

which has a Coulombic $-1/r$ behavior at large r , and (ii) a short-range soft-core potential

$$V_Y(r) = -\frac{2.0}{\sqrt{r^2 + 0.5}} e^{-0.41r}, \quad (4)$$

with a cutoff radius $r_c \approx 2.2$ a.u. The ground states of both potentials reproduce the ionization potential $I_p \approx 0.9$ a.u. of helium.

As a nontrivially structured target we study the simplest diatomic molecule: the molecular ion H_2^+ . It is modeled in two dimensions as described in Ref. [55] with the potential

$$V_{\text{H}_2^+}(\mathbf{r}) = -\sum_{j=1,2} \frac{1}{\sqrt{\mathbf{r}_j^2 + 0.5}}, \quad (5)$$

where $\mathbf{r}_j = \mathbf{r} - \mathbf{R}_j$ with \mathbf{R}_j being the positions of the nuclei. The nuclei are kept fixed during the action of the pulse at the equilibrium internuclear distance of $R = 2$ a.u. such that the H_2^+ electronic ground-state energy of ≈ -1.11 a.u. is reproduced. To obtain a system that is symmetric under the interchange of the forward and backward directions (invariant under reflection at the x axis) in dipole approximation, the

molecular axis can either be aligned parallel or perpendicular to the electric field.

B. Numerical solution of the TDSE in 2D

To calculate *ab initio* photoelectron momentum distributions for ionization, we perform numerical simulations of the TDSE. Here, we only summarize roughly the used scheme that was introduced and described in detail in Ref. [54].

The dynamics of the system is determined in leading order of $1/c$ by the nonrelativistic Hamiltonian

$$H = \frac{1}{2}[\mathbf{p} + \mathbf{A}(t)]^2 + \frac{z}{c}[\mathbf{p} + \mathbf{A}(t)] \cdot \mathbf{E}(t) + V(\mathbf{r}), \quad (6)$$

where we have used the expansion of the vector potential as given in Eq. (2). Applying a unitary transformation $U = \exp(-i\chi)$ with a Hermitian operator

$$\chi = \frac{z}{c} \left(\mathbf{p} \cdot \mathbf{A}(t) + \frac{1}{2} \mathbf{A}^2(t) \right) \quad (7)$$

to this initial system in Coulomb gauge and using the form invariance of the TDSE, $i\partial_t \tilde{\psi}(\mathbf{r}, t) = \tilde{H} \tilde{\psi}(\mathbf{r}, t)$, leads to the transformed Hamiltonian

$$\begin{aligned} \tilde{H} = & \frac{1}{2} \left[\mathbf{p} + \mathbf{A}(t) + \frac{\mathbf{e}_z}{c} \left(\mathbf{p} \cdot \mathbf{A}(t) + \frac{1}{2} \mathbf{A}^2(t) \right) \right]^2 \\ & + V \left(\mathbf{r} - \frac{z}{c} \mathbf{A}(t) \right). \end{aligned} \quad (8)$$

No direct coupling between the position and momentum operator appears in \tilde{H} . Hence, in the special case of vanishing potential, the introduced canonical momenta in the transformed system are conserved in contrast to the canonical momenta in the original system.

The resulting TDSE is solved numerically using the standard Fourier split-operator method [56] with a time step of $\Delta t = 0.005$ a.u. The space is divided into an inner region, where the complete Hamiltonian \tilde{H} is implemented, and an outer region, where the asymptotic tail of the long-range potentials is neglected [57]. The size of the numerical inner grid is 209 a.u. in x and 819 a.u. in z direction with spacings of $\Delta x = 0.1$ a.u. and $\Delta z = 0.2$ a.u. After the end of the pulse the photoelectron momentum distribution is obtained from the outer grid with a resolution of $\Delta p_x = 0.015$ a.u. and $\Delta p_z = 0.004$ a.u.

C. Low-frequency approximation beyond the dipole approximation

The quantum-mechanical calculation of the photoelectron momentum distributions requires the knowledge of the overlap between the time-evolved state of the system $U(t_f, t_0)\psi_0$ and the scattering state $|\psi_{\mathbf{p}}^{(-)}(t_f)\rangle$ corresponding to an asymptotic momentum \mathbf{p} :

$$M_{\mathbf{p}}(t_f) = \langle \psi_{\mathbf{p}}^{(-)}(t_f) | U(t_f, t_0) | \psi_0 \rangle. \quad (9)$$

The time-evolved field-free initial state of the system is a good approximation for the bound state in the presence of the field in length gauge [58,59]. Hence we transform our initial system, formulated in Coulomb gauge with the Hamiltonian H of Eq. (6), by using the unitary transformation

$U' = \exp[i\mathbf{A}(t) \cdot \mathbf{r}]$ to a modified ‘‘length’’ gauge form $H' = H_0 + H_I(t)$ involving the field-free Hamiltonian $H_0 = \mathbf{p}^2/2 + V(\mathbf{r})$ and the interaction operator

$$H_I(t) = \mathbf{E}(t) \cdot \left(\mathbf{r} + \frac{z}{c} \mathbf{p} \right). \quad (10)$$

The full time-evolution operator can be rewritten by using Dyson equations

$$U(t_f, t_0) = U_0(t_f, t_0) - i \int_{t_0}^{t_f} dt' U(t_f, t') H_I(t') U_0(t', t_0), \quad (11)$$

$$U(t_f, t') = U_F(t_f, t') - i \int_{t'}^{t_f} dt U_F(t_f, t) V U(t, t'). \quad (12)$$

Here, U_0 denotes the field-free time-evolution operator such that the time evolution of the initial state is simply given by $\psi_0(t') = U_0(t', t_0)\psi_0 = \exp[iE_0(t_0 - t')]\psi_0$. The propagator U_F corresponds to the potential-free Hamiltonian $H_F = \mathbf{p}^2/2 + H_I(t)$ that describes the time evolution of an electron in the electromagnetic field in leading order of $1/c$. It can be expressed

$$U_F(t, t') = \int d\mathbf{k} |\psi_{\mathbf{k}}^F(t)\rangle \langle \psi_{\mathbf{k}}^F(t')|, \quad (13)$$

in terms of nondipole Gordon-Volkov states [47]

$$|\psi_{\mathbf{k}}^F(t)\rangle = e^{-iS_F(\mathbf{k}, t)} |\mathbf{v}(\mathbf{k}, t)\rangle \quad (14)$$

consisting of plane waves $|\mathbf{v}\rangle$ with wave vector

$$\mathbf{v}(\mathbf{k}, t) = \mathbf{k} + \mathbf{A}(t) + \frac{\mathbf{e}_z}{c} \left(\mathbf{k} \cdot \mathbf{A}(t) + \frac{1}{2} \mathbf{A}^2(t) \right) \quad (15)$$

and a phase factor with the generalized action

$$S_F(\mathbf{k}, t) = \frac{1}{2} \int^t d\zeta \mathbf{v}^2(\mathbf{k}, \zeta). \quad (16)$$

Inserting Eq. (12) into Eq. (11) the S -matrix element (9) can be written as

$$M_{\mathbf{p}}(t_f) = M_{\mathbf{p}}^D(t_f) + M_{\mathbf{p}}^R(t_f), \quad (17)$$

with the amplitude for direct electrons

$$M_{\mathbf{p}}^D(t_f) = -i \int_{t_0}^{t_f} dt' \langle \psi_{\mathbf{p}}^{(-)}(t_f) | U_F(t_f, t') H_I(t') | \psi_0(t') \rangle \quad (18)$$

and the rescattering term

$$\begin{aligned} M_{\mathbf{p}}^R(t_f) = & (-i)^2 \int_{t_0}^{t_f} dt' \int_{t'}^{t_f} dt \langle \psi_{\mathbf{p}}^{(-)}(t_f) | U_F(t_f, t) \\ & \times V U(t, t') H_I(t') | \psi_0(t') \rangle. \end{aligned} \quad (19)$$

Up to this point no approximation has been made. If we restrict ourselves to direct electrons described by Eq. (18) and approximate the exact scattering state $|\psi_{\mathbf{p}}^{(-)}\rangle$ by a plane wave $|\mathbf{p}\rangle$ with the same final momentum \mathbf{p} , we obtain the ‘‘direct’’ SFA beyond the electric dipole approximation [52]. However, in this work we are interested in the high-energy region of the momentum distribution corresponding to rescattered electrons. If we replace the exact scattering state by a plane wave and the full time-evolution operator $U(t_f, t)$ by the Gordon-Volkov propagator $U_F(t_f, t)$ in the amplitude of ATI with rescattering, we retrieve the nondipole ISFA of Ref. [52].

Here, the laser-assisted scattering is treated in first Born approximation (1BA) such that the “distortion” of the incident plane wave $|\mathbf{v}(\mathbf{k}, t)\rangle$ caused by the potential is neglected.

The reliability of the ISFA is restricted by the accuracy of the 1BA which depends on the energy of the rescattering electron, the shape of the potential, and the dimensionality of the problem. Since in two dimensions even for a bare Coulomb potential the exact quantum-mechanical DCS and the 1BA only agree asymptotically for large energies, we include rescattering effects beyond the 1BA by means of a LFA [30]. The main idea is that in analogy with the three-step model the motion of the electron can be separated in different stages of potential-free acceleration of the ionized electron wave packet in the laser field and field-free potential scattering that changes the velocity from $\mathbf{v}(\mathbf{k}, t)$ to $\mathbf{v}(\mathbf{p}, t)$. The approximation to the full dynamics should work well if the change of the electron velocity $\mathbf{v}(\mathbf{k}, t)$ due to the laser field is small while the electron passes over the range of the potential [31]. To satisfy this condition the potential should have a much smaller support than the typical excursion amplitude of the electron in the laser field, which makes the approximation questionable for long-range potentials with Coulombic tail.

Mathematically, the LFA is an approximation to the laser-assisted scattering amplitude

$$R_{\mathbf{p},\mathbf{k}}(t, t') = \langle \psi_{\mathbf{p}}^F(t) | V U(t, t') | \psi_{\mathbf{k}}^F(t') \rangle, \quad (20)$$

which can be read off from Eq. (19). Following the derivation in Ref. [31] but including leading-order nondipole effects properly the scattering amplitude can be expanded in powers of the laser frequency ω . The zeroth-order term yields the LFA

$$R_{\mathbf{p},\mathbf{k}}^{\text{LFA}}(t, t') = \langle \psi_{\mathbf{p}}^F(t) | T_0(\tilde{E}(\mathbf{k}, t)) | \psi_{\mathbf{k}}^F(t') \rangle \quad (21)$$

with the “kinetic energy” of the laser-driven electron

$$\tilde{E}(\mathbf{k}, t) = \mathbf{v}^2(\mathbf{k}, t)/2. \quad (22)$$

Here, we introduced the field-free T operator for scattering off the potential V

$$T_0(E) = V + V G_V(E) V \quad (23)$$

and the stationary Green’s operator in the absence of the laser field

$$G_V(E) = (E - H_0 + i\epsilon)^{-1}, \quad \epsilon \rightarrow 0^+. \quad (24)$$

The T -matrix elements can be reexpressed

$$t(\mathbf{v}_{\text{out}}, \mathbf{v}_{\text{in}}) = \langle \mathbf{v}_{\text{out}} | T_0(E_{\text{in}}) | \mathbf{v}_{\text{in}} \rangle = \langle \mathbf{v}_{\text{out}} | V | \psi_{\mathbf{v}_{\text{in}}}^{(+)} \rangle \quad (25)$$

in terms of the field-free stationary scattering state $|\psi_{\mathbf{k}}^{(+)}\rangle$ [60]. Finally, we obtain an approximation for the amplitude of rescattered electrons

$$M_{\mathbf{p}}^{\text{LFA}}(t_f) = (-i)^2 \int_{t_0}^{t_f} dt' \int_{t'}^{t_f} dt \int d\mathbf{k} \times t(\mathbf{v}(\mathbf{p}, t), \mathbf{v}(\mathbf{k}, t)) D(\mathbf{k}, t') e^{iS_{\mathbf{p},\mathbf{k}}(t, t')} \quad (26)$$

with a matrix element describing the ionization

$$D(\mathbf{k}, t') = \langle \mathbf{v}(\mathbf{k}, t') | H_1(t') | \psi_0 \rangle \quad (27)$$

and the combined action

$$S_{\mathbf{p},\mathbf{k}}(t, t') = S_F(\mathbf{p}, t) - S_F(\mathbf{k}, t) + S_F(\mathbf{k}, t') + I_p t', \quad (28)$$

where the partial actions S_F defined in Eq. (16) are used. Since the calculation of the off-shell T -matrix elements is quite demanding, further approximations are desirable.

D. Saddle-point analysis

In the long-wavelength limit ($U_p > I_p \gg \omega$) the fivefold integral in Eq. (26) can be approximated by means of the saddle-point method. To this end the stationary points of the action S with respect to all appearing integration variables are searched for: $\partial_x S_{\mathbf{p},\mathbf{k}}(t, t') = 0$ with $x \in \{t', t, \mathbf{k}\}$. The saddle point \mathbf{k}_s corresponding to the momentum integration is determined in first order of $1/c$ by

$$0 = - \int_{t'_s}^{t_s} d\tau \left(\mathbf{v}(\mathbf{k}_s, \tau) + \frac{k_{s,z}}{c} \mathbf{A}(\tau) \right). \quad (29)$$

This equation can be analytically solved in first order of $1/c$,

$$\mathbf{k}_s \approx - \frac{\boldsymbol{\alpha}(t_s, t'_s)}{t_s - t'_s} + \frac{1}{c} \left(\frac{\alpha^2(t_s, t'_s)}{(t_s - t'_s)^2} - \frac{\alpha_2(t_s, t'_s)}{2(t_s - t'_s)} \right) \mathbf{e}_z, \quad (30)$$

with the integrals $\boldsymbol{\alpha}(t, t') = \int_{t'}^t d\tau \mathbf{A}(\tau)$ and $\alpha_2(t, t') = \int_{t'}^t d\tau \mathbf{A}^2(\tau)$. The first term of Eq. (30) is familiar from the dipole limit. The corrections point along the propagation direction of the light and represent classically the required initial velocity to compensate the drift motion of the electron due to the nondipole part of the Lorentz force.

The stationarity conditions with respect to the ionization time t'_s and the return time t_s lead to the relations

$$\tilde{E}(\mathbf{k}_s, t'_s) = -I_p, \quad (31)$$

$$\tilde{E}(\mathbf{k}_s, t_s) = \tilde{E}(\mathbf{p}, t_s). \quad (32)$$

Formally, these two conditions represent the energy conservation in the ionization process and the rescattering process. Efficient recollision requires an initial velocity with nonzero z component, which can be interpreted as giving rise to an increased effective ionization potential. This implies a reduced ionization rate [47,52] and forces the solutions to be complex even when $I_p = 0$. The energy conservation in the rescattering process reduces the T -matrix element to the scattering sphere defined by the energy of the incoming electron and hence it has only to be evaluated on shell. The T -matrix elements are calculated in two spatial dimensions as described in the Appendix.

The complex-valued ionization and return time t'_s, t_s are determined numerically after inserting the analytical form of the intermediate momentum \mathbf{k}_s from Eq. (30) in the system of Eqs. (31) and (32). For the used short laser pulse only two main branches of trajectories with travel times $\text{Re}(t_s - t'_s)$ less than one laser cycle give non-negligible contributions. The two trajectories are referred to as the “short” and “long” trajectory [61]. In the usual saddle-point approximation the integral in Eq. (26) is approximated by a sum over the relevant contributions corresponding to the different saddle-point solutions. However, close to the classical cutoff both solutions merge and beyond the long trajectory has to be skipped. Hence, for an adequate description of the whole rescattering plateau, we use the uniform approximation as described in Ref. [62].

The contribution of a single trajectory s to the rescattering amplitude is given by

$$M_{\mathbf{p},s}^{\text{LFA}} = (-i)^2 C t(\mathbf{v}(\mathbf{p}, t_s), \mathbf{v}(\mathbf{k}_s, t_s)) e^{iS_{\mathbf{p},\mathbf{k}_s}(t_s, t'_s)}, \quad (33)$$

with the prefactor C arising from the Hessian matrix

$$C = \sqrt{\frac{(2\pi i)^4}{\det(H_{t,t',\mathbf{k}}[S_{\mathbf{p},\mathbf{k}}(t, t')])}}. \quad (34)$$

Here, we have dropped the ionization matrix element D , which has a pole at the saddle points. Since both relevant trajectories start in a small time window close to $\text{Re}(t'_s) \approx T$, the prefactor for ionization arising from the matrix element D has only minor influence on the spectrum in HATI and can be neglected. For a Yukawa potential we found in IBA that the influence of the imaginary parts of the velocities entering the T -matrix element is negligible and hence they are also ignored in the calculation of all T -matrix elements. Following Ref. [61] we refer to the resulting model as quantum-orbit model (QOM).

III. RESULTS AND DISCUSSION

A. TDSE results

The asymptotic photoelectron momentum distribution from ionization of the molecular ion H_2^+ with a three-cycle laser pulse is shown in Fig. 1: (a) parallel and (b) perpendicular orientation of the molecular axis relative to the electric field. Both spectra show the same division into a strong contribution of low-energy electrons concentrated along the p_x axis and a weaker contribution of high-energy electrons, which extend over a large range of momenta p_z . Due to the shortness of the pulse, ATI peaks are avoided in the high-energy region [28] and the nearly circular ring structures which are caused by the interference between short and long rescattering trajectories [61,63] show a strong asymmetry between positive and negative p_x . The carrier envelope phase of the pulse in Eq. (1) is such that the rescattering electrons with the highest energy are emitted with positive momenta p_x and that their cutoff energy is close to the classical value of $E \approx 10U_p$ of a cw field [18,19]. For both orientations of H_2^+ the intensity distributions on top of the circular interference structure show a nontrivial structure-dependent variation compared to our work on helium [54]. For parallel alignment the signal is reduced along a line nearly parallel to the p_z axis at $p_x \approx 3$ a.u.; see Fig. 1(a). On the other hand, for perpendicular alignment, more pronounced minima are aligned parallel to the p_x axis; see Fig. 1(b). Previously, the intensity variation has been attributed to the double-slit interference occurring when the returning electrons are rescattered by the diatomic molecular ion [34,35]. In contrast to the dipole limit, the exact positions of the minima indicated by the red solid lines are not symmetric with respect to the polarization axis and offer the opportunity to observe directly the symmetry breaking in propagation direction (z direction). These shifts depend on p_x : close to the cutoff, larger shifts of around 0.12 a.u. are observed, whereas for smaller p_x , the minima are shifted by only ≈ 0.05 a.u.

As in our previous work on helium [54] we divide the observed deviations from the dipole approximation in

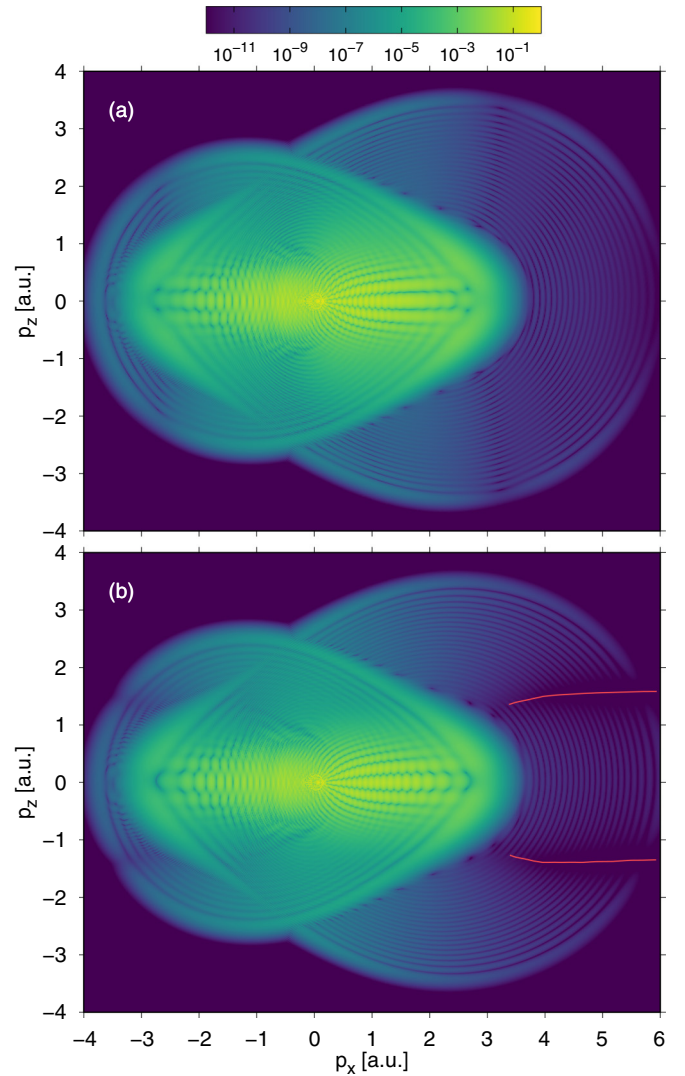


FIG. 1. Photoelectron momentum distribution $w(\mathbf{p})$ from ionization of H_2^+ with (a) parallel and (b) perpendicular orientation of the molecular axis relative to the electric field by a three-cycle pulse with 814 nm wavelength and peak intensity of 8×10^{14} W/cm². The red lines are the numerically determined positions of the interference minima.

two major classes: (i) the minima and maxima resulting from the interference between short and long trajectories are shifted in z direction, i.e., their positions are no longer symmetric about the polarization axis; (ii) also the strength of the peaks are different in forward and backward directions. In the following we refer to the second effect as *asymmetry*.

The momentum shifts extracted from the TDSE for the molecular ion H_2^+ are only hardly influenced by the alignment and in our numerical accuracy they are the same as for helium. This negligible dependence on the target structure is in perfect agreement with the classical interpretation given in Ref. [54]. There, it has been shown in a classical three-step model that the shift is caused by the acceleration of the electron in the electromagnetic field after the rescattering event. The gained additional momentum is equal to the energy

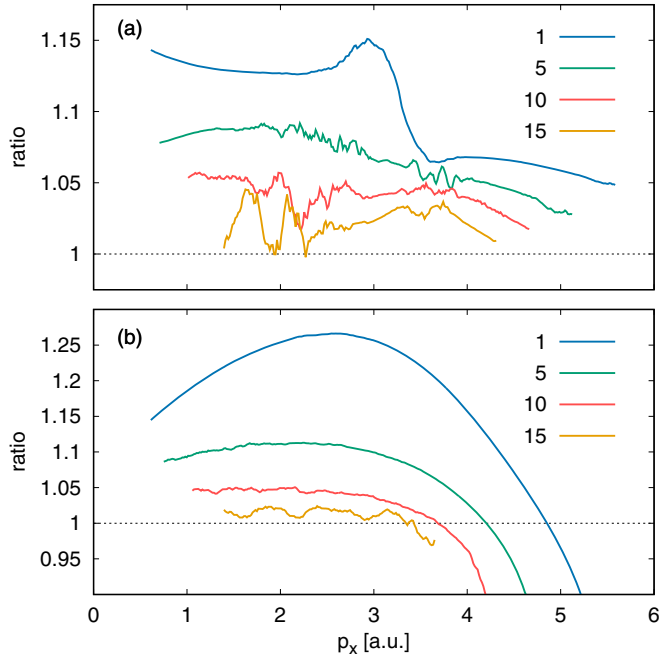


FIG. 2. Forward-backward asymmetry quantified as the ratio of the signal strengths in forward and backward directions for H_2^+ at (a) parallel and (b) perpendicular alignment. The panels show results for the interference rings 1, 5, 10, and 15 (from the top curve to the bottom curve), where the label “1” denotes the outermost ring.

gain after rescattering divided by the speed of light c and should only depend on the laser field.

On the other hand, the forward-backward asymmetry is quantified at each p_x by taking the ratio of the signals of one interference maximum in forward direction and one in backward direction, where each signal is obtained by p_z integration over one peak. In Fig. 2 the asymmetry extracted from the TDSE for H_2^+ is shown for selected interference rings. For example, the label “5” denotes the fifth interference ring when counting inwards. The asymmetry ratio depends strongly on the ring number such that its deviation from unity (where the signals in forward and backward directions are equally strong) gets smaller when moving to inner rings. The atomic or molecular structure is imprinted on the asymmetry ratio and especially its p_x dependence. For example, for H_2^+ aligned parallel to the electric field, the outer ring only shows positive ratios indicating a stronger emission in forward than in backward direction with a modulation feature around $p_x \approx 3$ a.u. In contrast, for the perpendicular alignment, a single maximum with values as high as ≈ 1.26 is observed that decreases strongly while going to higher momenta p_x such that an inverted asymmetry with stronger emission in backward direction is found for momenta p_x larger than ≈ 4.8 a.u. For the inner rings, e.g., ring number 15, a substructure is visible on top of the signal. We believe that it can be attributed to the following issues: (i) close to the center of the distribution the falling tail of the strong signal of direct electrons act as a background that leads to additional interference; (ii) in contrast to the outer rings the inner rings have a smaller modulation depth and hence the integration of the signal depends noticeably on the used integration limits.

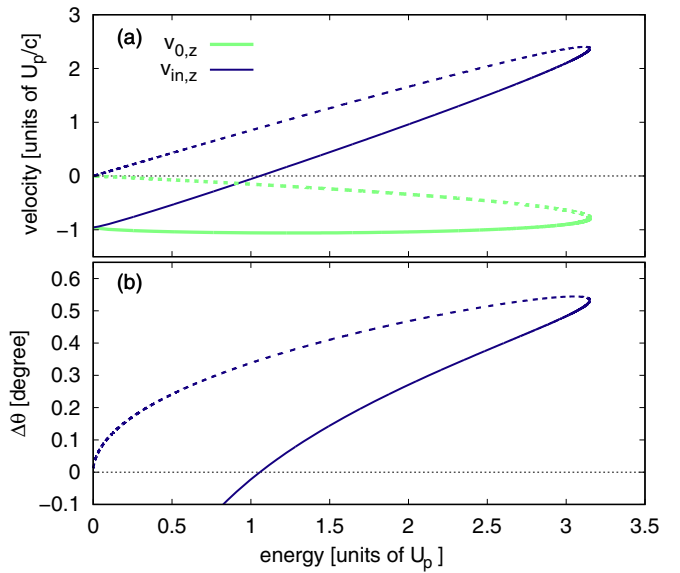


FIG. 3. (a) Initial velocity $v_{0,z}$ and z component of the incoming rescattering velocity $v_{in,z}$ as a function of the recollision energy in U_p for the classical model. (b) Offset angle $\Delta\theta$ of the incoming electron with respect to the polarization axis using the laser parameters of Fig. 1. The dashed lines correspond to short trajectories, whereas the solid lines correspond to long trajectories.

B. Generalized three-step model beyond the electric dipole approximation

To gain deeper physical insight we extend our classical model for HATI introduced in Ref. [54] by treating the scattering step more carefully. Mainly, this simple model follows the idea of the three-step model [19,21] that the motion of the electron can be split in different stages: (i) laser-induced ionization, (ii) acceleration of the electron away and back to the parent ion, and (iii) scattering off the ionic potential and further acceleration in the field. Additionally, leading-order nondipole effects are included.

After the ionization has launched an electron at the ionization time t_i , the potential-free acceleration of the electron is described classically by Newton’s equation. The magnetic part of the Lorentz force causes a drift motion of the electron in propagation direction. For an exact return to the initial position $\mathbf{r} = 0$ at the recollision time t_r and hence an efficient recollision process, the electron has to start with an initial velocity $\mathbf{v}_0 = -|v_0|\mathbf{e}_z$ against the propagation direction of the light [47]:

$$v_{0,z} = -\frac{1}{2c(t_r - t_i)} \int_{t_i}^{t_r} d\tau [\mathbf{A}(\tau) - \mathbf{A}(t_i)]^2. \quad (35)$$

Since long trajectories experience larger drifts compared to short trajectories, the magnitude of their initial velocities has to be larger; see Fig. 3(a). In first order of $1/c$, the resulting trajectory is only modified along the propagation direction of the light by the nondipole part of the Lorentz force. Hence the return condition in polarization direction, $x(t_i) = x(t_r)$, is the same as in the dipole limit and defines the mapping between the ionization time t_i and return time t_r .

For this potential-free trajectory starting from the position of the ion with initial velocity $\mathbf{v}_0 = -|v_0|\mathbf{e}_z$ we find in first order of $1/c$ a conserved canonical momentum of $\mathbf{k} = -\mathbf{A}(t_i) + \mathbf{A}^2(t_i)/(2c)\mathbf{e}_z + \mathbf{v}_0$ in the transformed system defined by the Hamiltonian of Eq. (8) without potential. The nondipole corrections to the intermediate momentum \mathbf{k} have the same form as in the classical limit of the QOM [compare Eq. (30)]. During the scattering the electron feels the potential and the canonical momentum is changed from \mathbf{k} to the momentum \mathbf{p} . If we assume that the influence of the potential on the further motion is negligible, the momentum \mathbf{p} is conserved and matches up with the measurable velocity. Close to the ionic core, $z \approx 0$, the connection between the classical velocity $\mathbf{v}(\kappa, t_r)$ of the electron and the conserved canonical momentum κ is given in first order of $1/c$ by Eq. (15). Hence the incoming velocity of the electron before the scattering event reads

$$\mathbf{v}_{\text{in}} = \mathbf{A}(t_r) - \mathbf{A}(t_i) + \frac{1}{2c}[\mathbf{A}(t_r) - \mathbf{A}(t_i)]^2 \mathbf{e}_z + \mathbf{v}_0. \quad (36)$$

For fixed times t_i, t_r the energy conservation during rescattering implies that the outgoing velocities $\mathbf{v}_{\text{out}} = \mathbf{v}(\mathbf{p}, t_r)$ after the scattering event lie on a circle of radius $K(t_r, t_i)$. Here, we have introduced the magnitude of the incoming velocity $K(t_r, t_i) \approx |\mathbf{A}(t_r) - \mathbf{A}(t_i)|$ that is in first order of $1/c$ the same as in the dipole limit. In our previous work [54] we have shown that the second stage of acceleration in the field maps the scattering circle of outgoing velocities onto an ellipse. In first order of $1/c$, its center is located at $\delta\mathbf{p} = -\mathbf{A}(t_r) + \mathbf{A}^2(t_r)/(2c)\mathbf{e}_z$ and the principal axes are rotated by 45° relative to the xz frame defined by light polarization and propagation.

For high kinetic energies of the incident electron such that the change of velocity due to the laser field is small while the electron passes over the nonzero part of the potential, we can neglect the influence of the laser field on the scattering process and assume field-free elastic scattering off the parent ion. Hence we approximate the corresponding scattering probability by the elastic scattering DCS

$$\sigma(K, \theta) \equiv \frac{dP}{d\Omega} \propto |t(\mathbf{v}_{\text{out}}, \mathbf{v}_{\text{in}})|^2. \quad (37)$$

For rotationally symmetric systems such as atoms the DCS depends only on the magnitude of the velocity K as well as the relative scattering angle $\theta = \angle(\mathbf{v}_{\text{out}}, \mathbf{v}_{\text{in}})$. In dipole approximation, where the motion during the first acceleration is confined on the polarization axis and hence the incoming velocity \mathbf{v}_{in} has no component in propagation direction, the scattering probability for opposite outgoing velocities $v_{\text{out},z}$ and $-v_{\text{out},z}$ at the same $v_{\text{out},x}$ are equal, i.e., the signal strength is symmetric about the polarization axis. However, taking nondipole effects into account the nonzero z component of the incoming velocity breaks the symmetry of the scattering probability with respect to the polarization axis. Instead, the DCS is rotated on the scattering circle by an angle $\Delta\theta \approx v_{\text{in},z}/v_{\text{in},x}$ with respect to the x axis. This symmetry breaking is schematically illustrated in Fig. 4.

The z component of the incoming rescattering velocity is positive for high return energies $K^2/2$; see Fig. 3(a). Close to the cutoff it is dominated by the momentum $K^2/(2c)$ transferred from the light field to the electron during its first

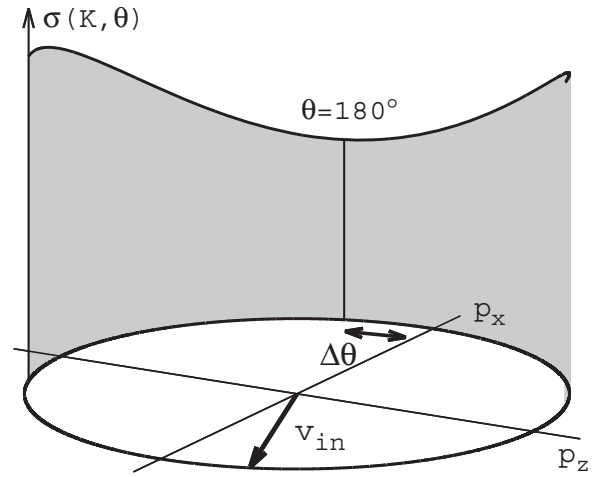


FIG. 4. Schematic sketch (with exaggerated value of $1/c$) of the scattering probability for an electron with incoming velocity \mathbf{v}_{in} . The black solid line in the p_x - p_z plane represents the scattering circle on which the possible outgoing velocities \mathbf{v}_{out} lie. Due to the nondipole part of the Lorentz force acting during the first acceleration, the incoming velocity is at an angle $\Delta\theta$ relative to the p_x axis and therefore the scattering probability is not symmetric about the p_x axis.

stage of acceleration; cf. Eq. (36). However, for a quantitative interpretation, the initial velocity \mathbf{v}_0 has to be taken into account, even though it is typically smaller by a factor of ≈ 4 . The resulting offset angle $\Delta\theta$ is mostly positive and has a maximum of $\approx 0.54^\circ$ for the given laser parameters; see Fig. 3(b). From Eq. (36) it follows that the z component of the incoming velocity scales quadratically with the electric-field strength E_0 and the wavelength λ . Since the x component varies linearly in both parameters, the offset angle $\Delta\theta$ is predicted to increase linearly with the field strength and the wavelength. During the recollision of the electron with the much heavier core an arbitrary amount of momentum can be exchanged. Since this exchange is determined by the DCS of the system, the asymmetry depends strongly on the used target gas and the scaling with the field parameters is not universal. For example, for a zero-range potential with its flat DCS [53] the asymmetry vanishes and hence the information on the incoming velocity is completely removed during the scattering. In contrast to the nondipole shift of the boundary, according to the three-step model the asymmetry can be completely attributed to the motion of the electron before rescattering and the rescattering process itself.

To compare the classical model and the TDSE results, we consider the short-range model of Eq. (4) for helium with cut-off radius $r_c \approx 2.2$ a.u. such that the region of non-negligible potential strength is small compared to the typical excursion amplitude of the electron estimated by $E_0/\omega^2 \approx 48$ a.u. for the used laser parameters. For the classical boundary, opposite points with the same p_x nearly belong to the same ellipse and hence differ only hardly in their ionization and return times. Thus we can neglect the influence of the ionization probability as well as the spread of the electron wave packet on the asymmetry. Hence we estimate the asymmetry as the ratio of the DCSs calculated on the classical boundary in forward

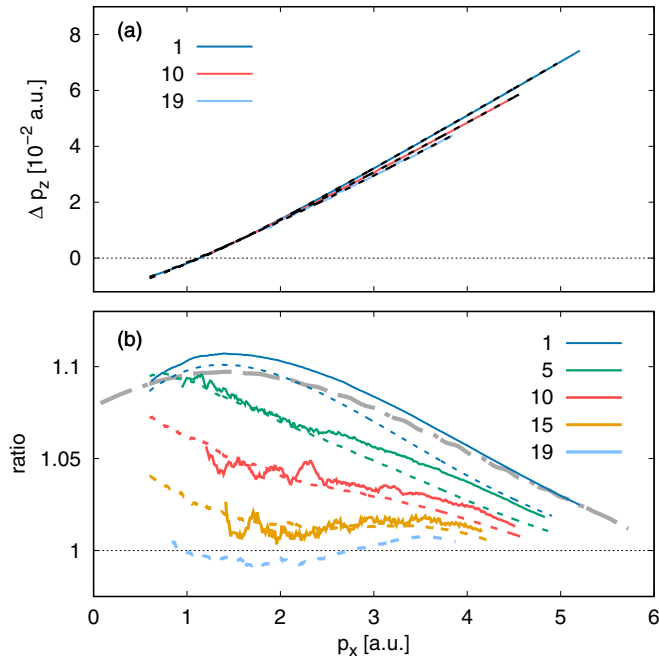


FIG. 5. (a) Shift of the interference maxima for the interference rings 1, 10, and 19 (from the top curve to the bottom curve): solid lines are numerical TDSE results; dashed thin lines are results from the QOM. (b) Forward-backward asymmetry quantified as the ratio of the interference pattern signal strength for the short-range potential: solid lines are numerical TDSE results; dashed thin lines are QOM results and long-dashed thick line is classical estimation obtained by calculating the ratio of the DCSs (see text for discussion). This panel shows results for interference rings 1, 5, 10, 15, and 19 (from top to bottom).

and backward directions. The result, shown in Fig. 5(b), is in good agreement with the exact asymmetry for the outer ring extracted from the TDSE calculation. In this special case, the DCS is (in the relevant energy region) a monotonically falling function of the return energy and the scattering angle θ between zero and 180° . The angle between the velocity of the incoming electron and the outgoing electron with positive $v_{\text{out},z}$ component is smaller than the angle for an outgoing electron with negative $v_{\text{out},z}$ component. Hence the scattering probability is higher in forward direction. This explains qualitatively the asymmetry ratios larger than one.

C. Comparison of the QOM and the numerical solution of TDSE

Since, in contrast to the outer ring, the interference between long and short trajectories strongly affects the signal strength for the inner rings, the quantum-orbit model (QOM) is used to interpret the spectra. Note that we include only the rescattering signal in the QOM results. Figure 6 shows 1D slices at $p_x = 1$ and 4 a.u. through the photoelectron momentum distribution for the short-range helium model calculated by solution of TDSE as well as within the QOM. Here, the QOM results have been rescaled such that they match the outer peaks of the TDSE results with positive p_z . For the slice at $p_x = 4$ a.u. the position of minima and maxima as well as the

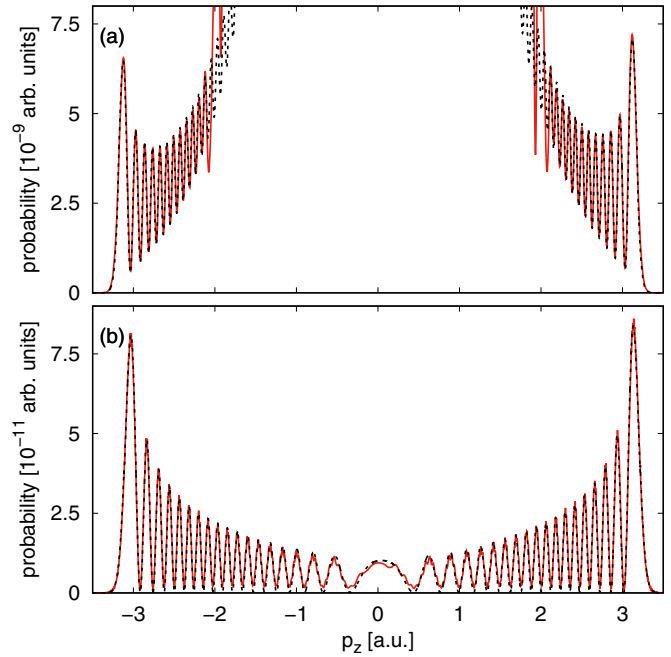


FIG. 6. Comparison of 1D slices through the 2D momentum distribution for the short-range potential at fixed p_x : (a) $p_x = 1.0$ a.u. and (b) $p_x = 4.0$ a.u. Shown are the exact numerical TDSE result (red solid line) and the QOM result (black dashed line).

overall shape of the spectrum are perfectly reproduced by the QOM. For smaller momenta p_x the distribution is still well reproduced close to the cutoff where rescattering electrons dominate. Closer to the p_x axis there are deviations. Naturally, in the region where “direct” electrons dominate, the QOM signal is completely off.

A reliable numerical value that quantifies the shifts of the interference peaks in light propagation direction is given by $\Delta p_z = (p_z^+ + p_z^-)/2$, where p_z^+ and p_z^- are the average values of p_z calculated over one peak in forward and one peak in backward direction, respectively. The shifts extracted from the QOM distributions are in perfect agreement with the exact TDSE results as seen in Fig. 5(a). Compared to the outer ring, the inner interference stripes show slightly smaller shifts. As the phase of the preexponential amplitude in Eq. (33) depends only weakly on the momentum \mathbf{p} , the appearance of the interference stripes can be mainly attributed to the difference of the action S between both trajectories [64]. However, close to the center of the plateau the absolute positions of the extrema are also influenced by the phases of the T -matrix elements that reach a difference of π for both rescattering trajectories. Substituting all expressions [except the phase $S_F(\mathbf{p}, t)$ accumulated after the scattering] by the corresponding expressions in dipole approximation and evaluating the resulting formula with the solutions of the saddle-point equations in the dipole limit leaves the location of the minima and maxima in the interference pattern nearly unchanged. Therefore, in agreement with the classical model, the shifts of the inner rings can be entirely attributed to the acceleration of the electron in the electromagnetic field after the rescattering event.

The asymmetry, calculated within the QOM using the same procedure as in TDSE, is compared to the exact results in Fig. 5(b) for selected interference rings. For the used short-range potential, the QOM results reproduce the overall trends when going to inner rings as well as the magnitude of the TDSE results. The observed difference between the classical result and the QOM in Fig. 5(b) can be completely attributed to the averaging over the whole interference stripe in the QOM calculation. As expected from the classical model an accurate description of the scattering step in terms of T -matrix elements is important. We have calculated the photoelectron distributions for some other short-range potentials (not shown), e.g., one with a structural minimum in the DCS as it is present in xenon. For all of them, the QOM model is able to reproduce the key features in the spectrum as well as in the extracted asymmetry.

As a final consistency check for our interpretation, we treat the dynamics after rescattering in the dipole limit. To correct for the different mappings of the outgoing velocities \mathbf{v}_{out} to the final momenta \mathbf{p} , we modify the action and solve the resulting saddle-point equations. We also insert the dipole energy in the T -matrix elements. Within these modifications, we can compare various observables directly to the calculations in the dipole limit. The obtained asymmetry is still in reasonable agreement with the full nondipole calculation (not shown) showing that only the modified incoming angle of the electron is responsible for the asymmetry in the signal strength. However, in the inner part of the rescattering plateau no simple interpretation of the asymmetry only in terms of the T -matrix elements is possible, because the rescattering velocities differ for long and short trajectories. This problem is well known from the reconstruction of DCSs in LIED carried out in QRS [30,32].

In order to quantitatively compare the QOM with exact results for long-range potentials with Coulombic tails, we concentrate on the long-range helium model. A slice through the momentum distribution at $p_x = 4.0$ a.u. is presented in Fig. 7(a). As for the short-range potential, the QOM result is rescaled such that the outer ring with positive p_z matches the TDSE result. Over the whole rescattering plateau the positions of interference extrema are well reproduced by the QOM, indicating that the difference in the sum of Coulomb phase and additional short-range phase between both relevant trajectories represents accurately the true phase difference accumulated due to the potential. However, the forward-backward asymmetry is only qualitatively modeled by the QOM as shown in Fig. 7(b). Especially the inversion of the ratio near $p_x = 3.3$ a.u. observed in the exact result is not visible in the QOM. The difference in absolute signal strength and in the modulation depth of the interference structure close to the center of the distribution can be at least partially attributed to Coulomb corrections of the ionization rate [65]. On the outer boundary, however, two points with the same p_x belong approximately to the same scattering event, so we believe that the Coulomb corrections of the ionization rate are not responsible for the deviations in the asymmetry. Rather, the long-range Coulombic tail influences the whole motion of the electron, especially the “propagation” in the continuum, and hence no clear separation between acceleration and rescattering is possible. To confirm that the Coulomb-laser coupling

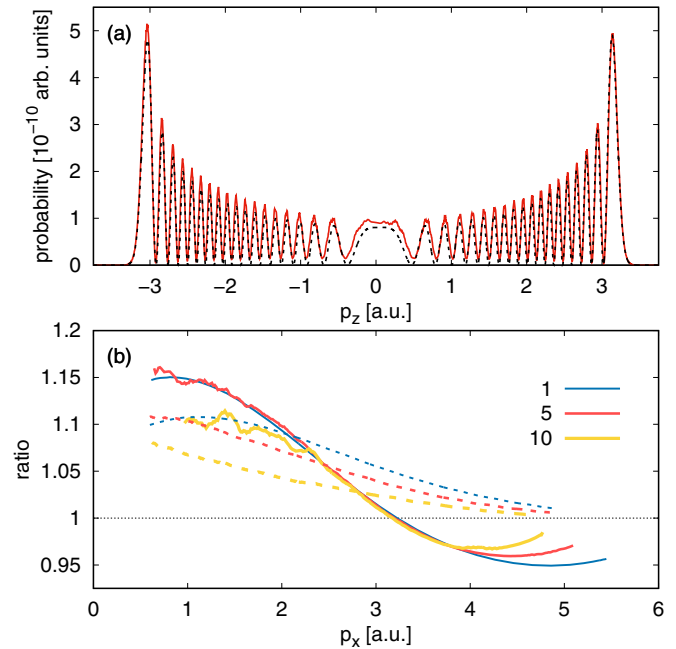


FIG. 7. (a) Comparison of 1D slices through the 2D momentum distribution for the long-range potential at fixed $p_x = 4.0$ a.u. Shown are the exact numerical TDSE result (red solid line) and the QOM result (black dashed line). (b) Corresponding forward-backward asymmetry quantified as the ratio of the interference pattern signal strength for the interference rings 1, 5, and 10: solid lines are numerical TDSE results; dashed lines are QOM results.

is important, we studied classical trajectories in the Coulomb potential, as used in classical Monte Carlo simulations. We found that, during the entire motion starting from the tunnel exit, the Coulomb potential changes not only the energy of the electron but also its direction, causing modifications in the scattering probability.

D. H_2^+ molecular ion: A simple model

In this section, we combine the classical rescattering model with a target-specific scattering DCS of H_2^+ in order to explain the TDSE results for H_2^+ . The prominent suppression in the HATI spectra for H_2^+ , shown in Fig. 1, is caused by destructive double-slit interference in the diatomic molecule [34,35]. There are four geometrical paths available to the recolliding electron depending on its initial position at one or the other center of the dimer as well as the center where the electron scatters off. It was shown in Ref. [66] that the matrix element related to the scattering process can be approximated by

$$t_{\text{H}_2^+}(\mathbf{v}_{\text{out}}, \mathbf{v}_{\text{in}}) \propto \cos\left(\frac{\mathbf{R} \cdot (\mathbf{v}_{\text{out}} - \mathbf{v}_{\text{in}})}{2}\right) t_{\text{H}}(\mathbf{v}_{\text{out}}, \mathbf{v}_{\text{in}}). \quad (38)$$

Here, the T -matrix element $t_{\text{H}}(\mathbf{v}_{\text{out}}, \mathbf{v}_{\text{in}})$ represents the elastic scattering of the electron off an atomic ion and it is calculated as described in the Appendix using a scattering potential with the shape of one of the terms in Eq. (5). In the cosine term, related to the interference, the explicit dependence on the molecular orientation defined by the molecular axis leads to scattering properties different from atoms where the

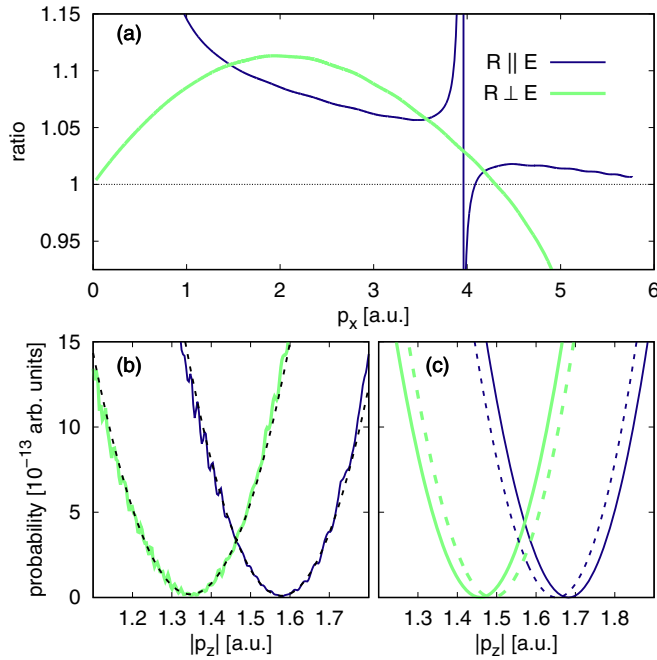


FIG. 8. (a) Asymmetry for H_2^+ at parallel or perpendicular alignment calculated within the classical model as the ratio of the DCSs from Eq. (38). (b) Signal on the classical boundary in the region of the two-center interference minimum at perpendicular alignment from the TDSE calculation for positive p_z (dark blue line) and negative p_z (light green line). The black dashed lines are the quadratic fits to determine precisely the positions of the minima. (c) Same as in (b) but calculated within the classical model. The solid lines correspond to the full calculation, whereas the dashed colored lines are calculated by neglecting the nondipole part of the incoming velocity \mathbf{v}_{in} .

T -matrix element only depends on the relative scattering angle θ . If only one trajectory dominates in the relevant region of the momentum distribution, the model predicts the following relation for the positions of the minima:

$$\mathbf{R} \cdot (\mathbf{v}_{\text{out}} - \mathbf{v}_{\text{in}}) = \pi. \quad (39)$$

We notice that the mapping of the outgoing velocity \mathbf{v}_{out} to the final momentum $\mathbf{p} = \mathbf{v}_{\text{out}} - \mathbf{A}(t_r) + 1/c[\mathbf{A}^2(t_r)/2 - v_{\text{out},x} A(t_r)]\mathbf{e}_z$ as well as the incoming velocity \mathbf{v}_{in} influence the exact positions.

For perpendicular alignment, the signal on the classical boundary interpolated from TDSE data is shown in Fig. 8(b) for momenta p_z close to the minima. From quadratic fits (black dashed lines) the positions of the minima are determined to $p_z \approx -1.347$ a.u. and $p_z \approx 1.578$ a.u. Both minima are shifted by ≈ 0.116 a.u. to larger p_z compared to the dipole limit where their position is given by $\approx \pm 1.463$ a.u. Even though the positions in the dipole limit $\pm\pi/2 \approx \pm 1.571$ a.u. predicted by the model of Eq. (39) are too large, the relative shift of ≈ 0.112 a.u. agrees well with the exact calculation; see Fig. 8(c). The combination of the shift of the classical boundary of about ≈ 0.082 a.u. and the z component of the incoming velocity of about ≈ 0.030 a.u. explain the shift of the structural minima compared to the dipole limit. In contrast to atomic targets, where the nondipole part of the incoming

velocity \mathbf{v}_{in} rotates the structures due to the DCS clockwise, for dimers at perpendicular orientation, the z component of the incoming velocity \mathbf{v}_{in} shifts the minima to larger p_z ; see Fig. 8(c).

For parallel alignment, according to the model of Eq. (39) only the x components of the incoming and outgoing velocities determine the interference minimum. Hence the nondipole part of the incoming velocity has no influence on the position of the minimum. Its p_x position is the same in forward and backward directions and agrees with the value from the dipole limit.

In Fig. 8(a) the asymmetry ratios for the outer inference ring calculated with the classical model of Sec. III B and the T -matrix elements of Eq. (38) are shown for both orientations of the molecule. Here, the main features of the exact results, shown in Fig. 2, are reproduced. For parallel alignment the modulation structure is much sharper in the model calculation which can be attributed to the deeper minimum. The structure appears because for fixed p_x two opposite points on the true classical boundary do not exactly belong to the same ellipse and hence do not have exactly the same DCS. For perpendicular alignment the inverted asymmetry for large momenta p_x is mainly caused by the nondipole part of the incoming velocity \mathbf{v}_{in} entering the \cos^2 interference factor of the DCS.

IV. CONCLUSIONS

We have analyzed HATI in atoms and diatomic molecules beyond the electric dipole approximation with a focus on the forward-backward asymmetry in the signal strength. We have first presented photoelectron momentum distributions from the numerical solution of the TDSE for the molecular ion H_2^+ in the high-energy rescattering regime. For perpendicular orientation of the molecular axis relative to the electric field and for the realistic laser parameters used in this work, the two-center interference minima in the rescattering plateau region are shifted by ≈ 0.11 a.u. to larger p_z compared to the dipole limit.

By including properly the rescattering step and the associated elastic differential cross section in the beyond dipole three-step model [54] we have studied the mechanisms underlying the forward-backward asymmetry for atomic targets. The drift of the electron during its first acceleration and the corresponding component in propagation direction of the incoming velocity before rescattering induce a scattering probability that is not symmetric about the polarization axis. In order to model the inner part of the plateau region with its interference pattern arising from long and short rescattering trajectories, we have extended the low-frequency approximation [30] beyond the dipole approximation and hence have approximated the laser-assisted scattering amplitude by the field-free scattering amplitude. For short-range potentials the corresponding quantum-orbit model offers a quantitative interpretation over the whole rescattering plateau. We have found that Coulomb effects in long-range potentials lead to modifications in the forward-backward asymmetry and hence prevent a simple analysis in terms of the elastic scattering differential cross section.

The nondipole shifts of the positions of the two-center interference minima for H_2^+ are well described by the

classical model. They become more pronounced with increasing laser intensity or wavelength. With the further development of midinfrared high-power lasers and the improvements in the experimental techniques it will be possible to observe the nondipole effects in the rescattering plateau. While the shift of interference structures resulting from long and short rescattering trajectories will be hard to detect after intensity averaging and the analysis of the asymmetry requires the knowledge of the deformed scattering ellipses, the broken symmetry should be directly observable in the two-center interference. We expect that the observed minima are, even after focal averaging [34], sufficiently pronounced to measure and analyze experimentally the underlying beyond dipole dynamics. If the positions of the minima are used to determine bond lengths and probe the nuclear dynamics, the neglect of nondipole corrections can lead to errors in the reconstructed lengths that have similar size as today's experimental accuracy [13].

ACKNOWLEDGMENTS

We thank Nicolas Eicke for useful discussions. S.B. thanks the Studienstiftung des deutschen Volkes for financial support.

APPENDIX: T -MATRIX ELEMENT

In this appendix we describe our method for the calculation of field-free scattering T -matrix elements in two dimensions for rotationally symmetric potentials $V(r)$. In the special case of short-range potentials the general theory has been invented in Ref. [67] and recently extended to asymptotically Coulomb-like potentials in Ref. [68]. We mainly follow the conventions introduced in Ref. [69].

For short-range potentials, the exact scattering states $\psi_{\mathbf{k}}^{(+)}$ with outgoing boundary conditions can be expanded in terms of partial waves $R_{E,m}(r)$

$$\psi_{\mathbf{k}}^{(+)}(\mathbf{r}) = \sum_{m=-\infty}^{\infty} i^m e^{i\delta_m} \frac{R_{E,m}(r)}{\sqrt{r}} e^{im(\theta_r - \theta_p)}, \quad (\text{A1})$$

with the energy-dependent scattering phases δ_m . Hence the partial waves have to fulfill the radial time-independent Schrödinger equation (TISE)

$$\left(-\frac{1}{2} \partial_r^2 + \frac{m^2 - 1/4}{2r^2} + V(r) - E \right) R_{E,m}(r) = 0. \quad (\text{A2})$$

This ordinary differential equation is integrated outwards on an equally spaced grid using the Numerov scheme. If we set $l = m - 1/2$, Eq. (A2) has the same form as in three dimensions. Therefore, in the special case of vanishing potential the solutions are given by the ordinary Bessel functions J_m, Y_m . From the asymptotic behavior at large distances r the phase shifts $\delta_m(E)$ can be read off from

$$\begin{aligned} \frac{R_{E,m}(r)}{\sqrt{r}} &\propto A J_m(kr) + B Y_m(kr) \\ &\propto \frac{1}{\sqrt{r}} \sin \left(kr - m \frac{\pi}{2} + \frac{\pi}{4} + \delta_m(E) \right) \end{aligned} \quad (\text{A3})$$

to $\tan(\delta_m(E)) = -B/A$. Asymptotically, the full scattering state consists of an incident plane wave and a scattered

circular outgoing wave

$$\psi_{\mathbf{k}}^{(+)}(\mathbf{r}) \simeq e^{i\mathbf{k}\cdot\mathbf{r}} + \sqrt{\frac{i}{k}} f_k(\theta) \frac{e^{ikr}}{\sqrt{r}}. \quad (\text{A4})$$

The introduced scattering amplitude f is directly proportional to the on-shell T -matrix element in elastic scattering theory

$$t(\mathbf{p}, \mathbf{k}) = \langle \mathbf{p} | V | \psi_{\mathbf{k}}^{(+)} \rangle \propto f_k(\theta) \quad (\text{A5})$$

and can be completely expressed in terms of scattering phase shifts

$$f_k(\theta) = \sqrt{\frac{2}{\pi}} \sum_{m=-\infty}^{\infty} e^{i\delta_m} \sin(\delta_m) e^{im\theta}, \quad (\text{A6})$$

with θ being the relative angle between the incoming momentum \mathbf{k} and the outgoing momentum \mathbf{p} .

We consider long-range potentials that are asymptotically Coulomb-like and hence can be divided into

$$V(r) = V_C(r) + V_S(r) \quad (\text{A7})$$

with the bare Coulomb interaction $V_C(r) = -Z/r$ and the short-range part $V_S(r)$. The asymptotic behavior of the scattering states is given by regular and irregular Coulomb functions F_l, G_l with index $l = m - 1/2$. In addition to the phase shift δ_m due to the short-range part V_S in the presence of the Coulomb potential two terms appear in the analog of Eq. (A3): one representing the Coulomb phase shift $\sigma_m = \arg \Gamma(m - 1/2 + i\gamma)$ with the Sommerfeld parameter $\gamma = -Z/k$ and another $-\gamma \ln(2kr)$ representing the long-range nature of the potential, in the sense that plane waves do not asymptotically become the solutions of the TISE.

Analogous to three dimensions the resulting scattering amplitude can be divided into

$$f_k(\theta) = f_k^C(\theta) + f_k^S(\theta), \quad (\text{A8})$$

where

$$f_k^C(\theta) = -\frac{\gamma}{\sqrt{2} \sin^2(\theta/2)} \frac{\Gamma(1/2 + i\gamma)}{\Gamma(1 - i\gamma)} e^{-i\gamma \ln[\sin^2(\theta/2)]} \quad (\text{A9})$$

is the Coulomb scattering amplitude in two dimensions [70] and

$$f_k^S(\theta) = \frac{1}{2i} \sqrt{\frac{2}{\pi}} \sum_{m=-\infty}^{\infty} e^{2i\sigma_m} [e^{2i\delta_m} - 1] e^{im\theta} \quad (\text{A10})$$

is the additional scattering amplitude due to the short-range part V_S in the presence of the Coulomb potential V_C .

In order to check the derived separation in Eq. (A8), we truncated smoothly the long-range potential at a large distance $r \approx 100$ a.u. and calculated the DCS with the theory for short-range potentials. Both results are in perfect agreement for the relevant energies above ≈ 0.125 a.u.

- [1] M. Lein, Molecular imaging using recolliding electrons, *J. Phys. B* **40**, R135 (2007).
- [2] H. Niikura, F. Légaré, R. Hasbani, A. D. Bandrauk, M. Y. Ivanov, D. M. Villeneuve, and P. B. Corkum, Sub-laser-cycle electron pulses for probing molecular dynamics, *Nature (London)* **417**, 917 (2002).
- [3] J. Itatani, J. Levesque, D. Zeidler, H. Niikura, H. Pépin, J. C. Kieffer, P. B. Corkum, and D. M. Villeneuve, Tomographic imaging of molecular orbitals, *Nature (London)* **432**, 867 (2004).
- [4] S. Baker, J. S. Robinson, C. A. Haworth, H. Teng, R. A. Smith, C. C. Chirilă, M. Lein, J. W. G. Tisch, and J. P. Marangos, Probing proton dynamics in molecules on an attosecond time scale, *Science* **312**, 424 (2006).
- [5] O. Smirnova, Y. Mairesse, S. Patchkovskii, N. Dudovich, D. Villeneuve, P. B. Corkum, and M. Y. Ivanov, High harmonic interferometry of multi-electron dynamics in molecules, *Nature (London)* **460**, 972 (2009).
- [6] P. M. Kraus, B. Mignolet, D. Baykusheva, A. Rupenyany, L. Horný, E. F. Penka, G. Grassi, O. I. Tolstikhin, J. Schneider, F. Jensen, L. B. Madsen, A. D. Bandrauk, F. Remacle, and H. J. Wörner, Measurement and laser control of attosecond charge migration in ionized iodoacetylene, *Science* **350**, 790 (2015).
- [7] A. T. Eppink and D. H. Parker, Velocity map imaging of ions and electrons using electrostatic lenses: Application in photoelectron and photofragment ion imaging of molecular oxygen, *Rev. Sci. Instrum.* **68**, 3477 (1997).
- [8] R. Dörner, V. Mergel, O. Jagutzki, L. Spielberger, J. Ullrich, R. Moshhammer, and H. Schmidt-Böcking, Cold target recoil ion momentum spectroscopy: A momentum microscope to view atomic collision dynamics, *Phys. Rep.* **330**, 95 (2000).
- [9] T. Zuo, A. D. Bandrauk, and P. B. Corkum, Laser-induced electron diffraction: A new tool for probing ultrafast molecular dynamics, *Chem. Phys. Lett.* **259**, 313 (1996).
- [10] M. Lein, J. P. Marangos, and P. L. Knight, Electron diffraction in above-threshold ionization of molecules, *Phys. Rev. A* **66**, 051404(R) (2002).
- [11] D. Ray, B. Ulrich, I. Bocharova, C. Maharjan, P. Ranitovic, B. Gramkow, M. Magrakvelidze, S. De, I. V. Litvinyuk, A. T. Le, T. Morishita, C. D. Lin, G. G. Paulus, and C. L. Cocke, Large-Angle Electron Diffraction Structure in Laser-Induced Rescattering from Rare Gases, *Phys. Rev. Lett.* **100**, 143002 (2008).
- [12] M. Meckel, D. Comtois, D. Zeidler, A. Staudte, D. Pavičić, H. C. Bandulet, H. Pépin, J. C. Kieffer, R. Dörner, D. M. Villeneuve, and P. B. Corkum, Laser-induced electron tunneling and diffraction, *Science* **320**, 1478 (2008).
- [13] C. I. Blaga, J. Xu, A. D. DiChiara, E. Sistrunk, K. Zhang, P. Agostini, T. A. Miller, L. F. DiMauro, and C. D. Lin, Imaging ultrafast molecular dynamics with laser-induced electron diffraction, *Nature (London)* **483**, 194 (2012).
- [14] S. G. Walt, N. Bhargava Ram, M. Atala, N. I. Shvetsov-Shilovski, A. von Conta, D. Baykusheva, M. Lein, and H. J. Wörner, Dynamics of valence-shell electrons and nuclei probed by strong-field holography and rescattering, *Nat. Commun.* **8**, 15651 (2017).
- [15] P. Agostini, F. Fabre, G. Mainfray, G. Petite, and N. K. Rahman, Free-Free Transitions Following Six-Photon Ionization of Xenon Atoms, *Phys. Rev. Lett.* **42**, 1127 (1979).
- [16] T. F. Gallagher, Above-Threshold Ionization in Low-Frequency Limit, *Phys. Rev. Lett.* **61**, 2304 (1988).
- [17] P. B. Corkum, N. H. Burnett, and F. Brunel, Above-Threshold Ionization in the Long-Wavelength Limit, *Phys. Rev. Lett.* **62**, 1259 (1989).
- [18] G. G. Paulus, W. Becker, W. Nicklich, and H. Walther, Rescattering effects in above-threshold ionization: A classical model, *J. Phys. B* **27**, L703 (1994).
- [19] G. G. Paulus, W. Nicklich, H. Xu, P. Lambropoulos, and H. Walther, Plateau in Above Threshold Ionization Spectra, *Phys. Rev. Lett.* **72**, 2851 (1994).
- [20] K. C. Kulander, K. J. Schafer, and J. L. Krause, Dynamics of short-pulse excitation, ionization and harmonic conversion, in *Super-Intense Laser-Atom Physics*, edited by B. Pireaux, A. L'Hullier, and K. Rzażewski, NATO ASI, Series B: Physics (Springer, Boston, MA, 1993), Vol. 316.
- [21] P. B. Corkum, Plasma Perspective on Strong Field Multiphoton Ionization, *Phys. Rev. Lett.* **71**, 1994 (1993).
- [22] L. V. Keldysh, Ionization in the field of a strong electromagnetic wave, *Sov. Phys. JETP* **20**, 1307 (1965).
- [23] F. H. M. Faisal, Multiple absorption of laser photons by atoms, *J. Phys. B* **6**, L89 (1973).
- [24] H. R. Reiss, Effect of an intense electromagnetic field on a weakly bound system, *Phys. Rev. A* **22**, 1786 (1980).
- [25] W. Becker, A. Lohr, and M. Kleber, Effects of rescattering on above-threshold ionization, *J. Phys. B* **27**, L325 (1994).
- [26] A. Lohr, M. Kleber, R. Kopold, and W. Becker, Above-threshold ionization in the tunneling regime, *Phys. Rev. A* **55**, R4003(R) (1997).
- [27] P. Salières, B. Carré, L. Le Déroff, F. Grasbon, G. G. Paulus, H. Walther, R. Kopold, W. Becker, D. B. Milošević, A. Sanpera, and M. Lewenstein, Feynman's path-integral approach for intense-laser-atom interactions, *Science* **292**, 902 (2001).
- [28] D. B. Milošević, G. G. Paulus, D. Bauer, and W. Becker, Above-threshold ionization by few-cycle pulses, *J. Phys. B* **39**, R203 (2006).
- [29] N. M. Kroll and K. M. Watson, Charged-particle scattering in the presence of a strong electromagnetic wave, *Phys. Rev. A* **8**, 804 (1973).
- [30] A. Čerkić, E. Hasović, D. B. Milošević, and W. Becker, High-order above-threshold ionization beyond the first-order Born approximation, *Phys. Rev. A* **79**, 033413 (2009).
- [31] D. B. Milošević, Low-frequency approximation for above-threshold ionization by a laser pulse: Low-energy forward rescattering, *Phys. Rev. A* **90**, 063423 (2014).
- [32] T. Morishita, A. T. Le, Z. Chen, and C. D. Lin, Accurate Retrieval of Structural Information from Laser-Induced Photoelectron and High-Order Harmonic Spectra by Few-Cycle Laser Pulses, *Phys. Rev. Lett.* **100**, 013903 (2008).
- [33] Z. Chen, A. T. Le, T. Morishita, and C. D. Lin, Origin of species dependence of high-energy plateau photoelectron spectra, *J. Phys. B* **42**, 061001 (2009).
- [34] M. Busuladžić, A. Gazibegović-Busuladžić, D. B. Milošević, and W. Becker, Angle-Resolved High-Order Above-Threshold Ionization of a Molecule: Sensitive Tool for Molecular Characterization, *Phys. Rev. Lett.* **100**, 203003 (2008).
- [35] M. Okunishi, R. Itaya, K. Shimada, G. Prümper, K. Ueda, M. Busuladžić, A. Gazibegović-Busuladžić, D. B. Milošević, and W. Becker, Two-Source Double-Slit Interference in Angle-

- Resolved High-Energy Above-Threshold Ionization Spectra of Diatoms, *Phys. Rev. Lett.* **103**, 043001 (2009).
- [36] C. T. L. Smeenk, L. Arissian, B. Zhou, A. Mysyrowicz, D. M. Villeneuve, A. Staudte, and P. B. Corkum, Partitioning of the Linear Photon Momentum in Multiphoton Ionization, *Phys. Rev. Lett.* **106**, 193002 (2011).
- [37] A. Ludwig, J. Maurer, B. W. Mayer, C. R. Phillips, L. Gallmann, and U. Keller, Breakdown of the Dipole Approximation in Strong-Field Ionization, *Phys. Rev. Lett.* **113**, 243001 (2014).
- [38] J. Maurer, B. Willenberg, J. Daněk, B. W. Mayer, C. R. Phillips, L. Gallmann, M. Klaiber, K. Z. Hatsagortsyan, C. H. Keitel, and U. Keller, Probing the ionization wave packet and recollision dynamics with an elliptically polarized strong laser field in the nondipole regime, *Phys. Rev. A* **97**, 013404 (2018).
- [39] S. Chelkowski, A. D. Bandrauk, and P. B. Corkum, Photon-momentum transfer in multiphoton ionization and in time-resolved holography with photoelectrons, *Phys. Rev. A* **92**, 051401(R) (2015).
- [40] I. A. Ivanov, J. Dubau, and K. T. Kim, Nondipole effects in strong-field ionization, *Phys. Rev. A* **94**, 033405 (2016).
- [41] A. S. Titi and G. W. F. Drake, Quantum theory of longitudinal momentum transfer in above-threshold ionization, *Phys. Rev. A* **85**, 041404(R) (2012).
- [42] M. Klaiber, E. Yakaboylu, H. Bauke, K. Z. Hatsagortsyan, and C. H. Keitel, Under-the-Barrier Dynamics in Laser-Induced Relativistic Tunneling, *Phys. Rev. Lett.* **110**, 153004 (2013).
- [43] E. Yakaboylu, M. Klaiber, H. Bauke, K. Z. Hatsagortsyan, and C. H. Keitel, Relativistic features and time delay of laser-induced tunnel ionization, *Phys. Rev. A* **88**, 063421 (2013).
- [44] H. R. Reiss, Relativistic effects in nonrelativistic ionization, *Phys. Rev. A* **87**, 033421 (2013).
- [45] P. L. He, D. Lao, and F. He, Strong Field Theories Beyond Dipole Approximations in Nonrelativistic Regimes, *Phys. Rev. Lett.* **118**, 163203 (2017).
- [46] Th. Keil and D. Bauer, Coulomb-corrected strong-field quantum trajectories beyond dipole approximation, *J. Phys. B* **50**, 194002 (2017).
- [47] M. W. Walser, C. H. Keitel, A. Scrinzi, and T. Brabec, High Harmonic Generation Beyond the Electric Dipole Approximation, *Phys. Rev. Lett.* **85**, 5082 (2000).
- [48] D. B. Milošević, S. Hu, and W. Becker, Quantum-mechanical model for ultrahigh-order harmonic generation in the moderately relativistic regime, *Phys. Rev. A* **63**, 011403(R) (2000).
- [49] N. J. Kylstra, R. M. Potvliege, and C. J. Joachain, Photon emission by ions interacting with short intense laser pulses: Beyond the dipole approximation, *J. Phys. B* **34**, L55 (2001).
- [50] C. C. Chirilă, N. J. Kylstra, R. M. Potvliege, and C. J. Joachain, Nondipole effects in photon emission by laser-driven ions, *Phys. Rev. A* **66**, 063411 (2002).
- [51] Y. I. Salamin, S. X. Hu, K. Z. Hatsagortsyan, and C. H. Keitel, Relativistic high-power laser matter interactions, *Phys. Rep.* **427**, 41 (2006).
- [52] M. Klaiber, K. Z. Hatsagortsyan, and C. H. Keitel, Above-threshold ionization beyond the dipole approximation, *Phys. Rev. A* **71**, 033408 (2005).
- [53] M. Klaiber, K. Z. Hatsagortsyan, and C. H. Keitel, Fully relativistic laser-induced ionization and recollision processes, *Phys. Rev. A* **75**, 063413 (2007).
- [54] S. Brennecke and M. Lein, High-order above-threshold ionization beyond the electric dipole approximation, *J. Phys. B* **51**, 094005 (2018).
- [55] M. Lein, P. P. Corso, J. P. Marangos, and P. L. Knight, Orientation dependence of high-order harmonic generation in molecules, *Phys. Rev. A* **67**, 023819 (2003).
- [56] M. D. Feit and J. A. Fleck, Jr., Solution of the Schrödinger equation by a spectral method II: Vibrational energy levels of triatomic molecules, *J. Chem. Phys.* **78**, 301 (1983).
- [57] M. Lein, E. K. U. Gross, and V. Engel, Intense-Field Double Ionization of Helium: Identifying the Mechanism, *Phys. Rev. Lett.* **85**, 4707 (2000).
- [58] D. Bauer, D. B. Milošević, and W. Becker, Strong-field approximation for intense-laser-atom processes: The choice of gauge, *Phys. Rev. A* **72**, 023415 (2005).
- [59] N. Eicke and M. Lein, Trajectory-free ionization times in strong-field ionization, *Phys. Rev. A* **97**, 031402(R) (2018).
- [60] J. R. Taylor, *Scattering Theory* (John Wiley & Sons, New York, 1972).
- [61] R. Kopold, D. B. Milošević, and W. Becker, Rescattering Processes for Elliptical Polarization: A Quantum Trajectory Analysis, *Phys. Rev. Lett.* **84**, 3831 (2000).
- [62] C. Figueira de Morisson Faria, H. Schomerus, and W. Becker, High-order above-threshold ionization: The uniform approximation and the effect of the binding potential, *Phys. Rev. A* **66**, 043413 (2002).
- [63] G. G. Paulus, F. Grasbon, A. Dreischuh, H. Walther, R. Kopold, and W. Becker, Above-Threshold Ionization by an Elliptically Polarized Field: Interplay between Electronic Quantum Trajectories, *Phys. Rev. Lett.* **84**, 3791 (2000).
- [64] M. Spanner, O. Smirnova, P. B. Corkum, and M. Y. Ivanov, Reading diffraction images in strong field ionization of diatomic molecules, *J. Phys. B* **37**, L243 (2004).
- [65] O. Smirnova, M. Spanner, and M. Ivanov, Analytical solutions for strong field-driven atomic and molecular one- and two-electron continua and applications to strong-field problems, *Phys. Rev. A* **77**, 033407 (2008).
- [66] E. Hasović, A. Gazibegović-Busuladžić, M. Busuladžić, D. B. Milošević, and W. Becker, High-order above-threshold ionization with few-cycle laser pulses: Molecular improved strong-field approximation vs. molecular low-frequency approximation, *Laser Phys.* **22**, 1819 (2012).
- [67] I. R. Lapidus, Quantum mechanical scattering in two dimensions, *Am. J. Phys.* **50**, 45 (1982).
- [68] V. V. Pupsyshev, The method of amplitude functions in two-dimensional scattering theory, *Theor. Math. Phys.* **191**, 499 (2017).
- [69] S. K. Adhikari, Quantum scattering in two dimensions, *Am. J. Phys.* **54**, 362 (1986).
- [70] G. Barton, Rutherford scattering in two dimensions, *Am. J. Phys.* **51**, 420 (1983).